Check for updates

# Tire appearance defect detection method *via* combining HOG and LBP features

Hongbin Liu*, Xinghao Jia, Chenhui Su, Hongjuan Yang and Chengdong Li

Shandong Key Laboratory of Intelligent Buildings Technology, School of Information and Electrical Engineering, Shandong Jianzhu University, Jinan, China

Tire appearance defect detection based on machine vision is an effective technology to improve the tire production quality. The detection process can be completed by the way of non-destructive testing. Therefore, more and more researchers are paying attention to this technology. However, tires are characterized by single block colors and various defects. It is a great challenge to accurately detect tire appearance defects. To complete the task of detecting tire defects, this paper presents a novel tire appearance defect detection method *via* combining histogram of oriented gradients (HOG) and local binary pattern (LBP) features. First, we construct a tire image dataset to provide defective and normal tire images. Then, histogram of oriented gradients and local binary pattern features of tire images are, respectively, extracted and used to train the support vector machine (SVM) classifier. Finally, the support vector machine classifier calculates the prediction scores of the test images *via* combining the histogram of oriented gradients and local binary pattern features. These scores can be utilized to determine whether the test image is a defective or a normal tire image, and the goal of tire appearance defect detection is achieved. Conducted on the tire image dataset, our method has verified the effectiveness of detecting tire detects, and the mean accuracy is improved more than 1.6% than the algorithm that only uses the histogram of oriented gradients or local binary pattern feature. The experimental results demonstrate that the combination of HOG and LBP features can increase tire appearance defect detection accuracy.

KEYWORDS

tire appearance, defect detection, non-destructive testing, feature fusion, image feature

## 1 Introduction

In recent years, the number of cars owned by residents has increased rapidly. The tire is one of the most important parts of cars, and it is necessary to ensure the surface quality of the tire because it directly affects the safety of drivers' lives. Therefore, the inspection of tire quality has become the focus in car manufacturing. The study of detecting tire appearance defects has excellent practical significance.

The tire production process is complicated and requires highly environmental and technological conditions. Tires in the high-speed production process often appear with a variety of minor defects, such as bubbles, peeling, impurities, bulging, and cracks. At the same time, most enterprises still use manual defect inspection according to personal experience; thus, some small defects cannot be effectively detected [1]. Moreover, the workload and work intensity of the workers are huge, and they are prone to misjudge easily when their eyes are fatigued [2, 3]. It is necessary to realize automatic and reliable inspection of tire appearance

defects, and the accurate detection method is important to reduce labor costs and improve the tire quality.

To achieve the goal of tire appearance defect detection with machine vision, many researchers analyze edges and texture features of defects [4]. For example, [5, 6] propose a multi-scale edge detection method for tires based on the Fourier transform analysis and wavelet transform. This method obtains wavelet filter coefficients according to the analysis of tire image characteristics to improve the accuracy of graphic edge detection and obtains better edge detection results. Research [7–10] was conducted to using Gabor filtering or other methods to process artificial features to realize simple and effective tire appearance defect detection.

Some methods utilize X-ray images to detect tire defects. Chuanwen Lin et al. [11] introduced a novel method for shoulder bending detection in tire X-ray images. They present a seed searching algorithm to find the defect, and the method obtains higher precision and recall. Research[3] shows a new defect detection algorithm for the image of the tire. It uses the Faster R-CNN network of the deep learning algorithm, which overcomes the shortcomings of traditional defect detection algorithms that require human involvement to extract defect features. Jinyin Chen et al. [12] put forward a novel deep learning model and modified the Faster R-CNN to conduct X-ray defect detection. However, X-ray images used in these methods require expensive image acquisition equipment.

Convolutional neural network (CNN) models [13–18] have also been widely applied in tire appearance defect detection. Sofia Sa'idah et al. [19] detected tire defects using the CNN method with GoogLeNet architecture. This study uses secondary data obtained from the Kaggle web dataset and produces high accuracy. Zhouzhou Zheng et al. proposed a novel two-stage convolutional neural network (CNN) [20] and an end-to-end residual U-structure (HLU$^2$-Net) [21] for tire defect detection. In HLU$^2$-Net, the novel residual U-structure is used to replace the encode–decode block of U-Net for fusing multi-scale and multi-level features. Although the accuracy of the CNN model is high, the computational cost is also large.

To develop the simple and effective tire defect detection in the industrial field, we present a tire appearance defect detection method based on HOG and LBP features. First, the tire appearance defect detection dataset is constructed, which consists of normal and defective tire images. Then, after preprocessing the images in the dataset, our method extracts HOG and LBP features of the tire image, and the feature model is established by training SVM classifiers. Finally, the SVM classifier predicts whether there are defects in the tire image by fusing HOG and LBP features. The motivation of our method is that the HOG feature represents edge information and the LBP feature describes the texture feature of the tire appearance; thus, the fusion of these two features can consider edge and texture features synthetically, which is beneficial in improving the accuracy of defect detection. HOG and LBP features are representative descriptors for representing edge features and texture features, which have been applied in many other fields. The experimental results show that our proposed defect detection method can effectively and accurately identify crack defects. The main work and innovations of this paper are as follows:

1) A tire appearance defect detection dataset is constructed. The dataset collects 1,021 images that consist of normal and defective tire images.

2) We present a tire defect detection method *via* combining HOG and LBP features. The method considers HOG and LBP features comprehensively. HOG and LBP features describe edge and texture information on the tire image, respectively. Therefore, the fusion of HOG and LBP features is beneficial for improving the defect detection ability.

3) The experiments compare our method to the algorithms that use the HOG or LBP feature alone. The results show that the accuracy of fusing HOG and LBP features to detect tire appearance defects is higher than the accuracy of using HOG or LBP features alone.

# 2 Tire appearance defect detection method *via* combining HOG and LBP features

## 2.1 Overview of the proposed method

The overall flowchart of our proposed tire appearance defect detection method is shown in Figure 1. First, we collect tire images and obtain a dataset that consists of normal and defective images. Second, our method preprocesses the normal and defective images, and then, HOG and LBP features of tire images are extracted to describe the tire's edge and texture information. Then, SVM classifiers are trained with HOG and LBP features, respectively. Afterward, the SVM classifier predicts the defective probability of the tire image with feature fusion by adding SVM predictive scores of HOG and LBP features. Finally, tire images are classified into normal or defective images.

## 2.2 Construction of the tire image dataset

We construct a tire image dataset to effectively detect tire defects. A total of 1,021 tire pictures are obtained by collecting industrial field and network screenshots, including 530 defective tire pictures and 491 normal tire pictures.
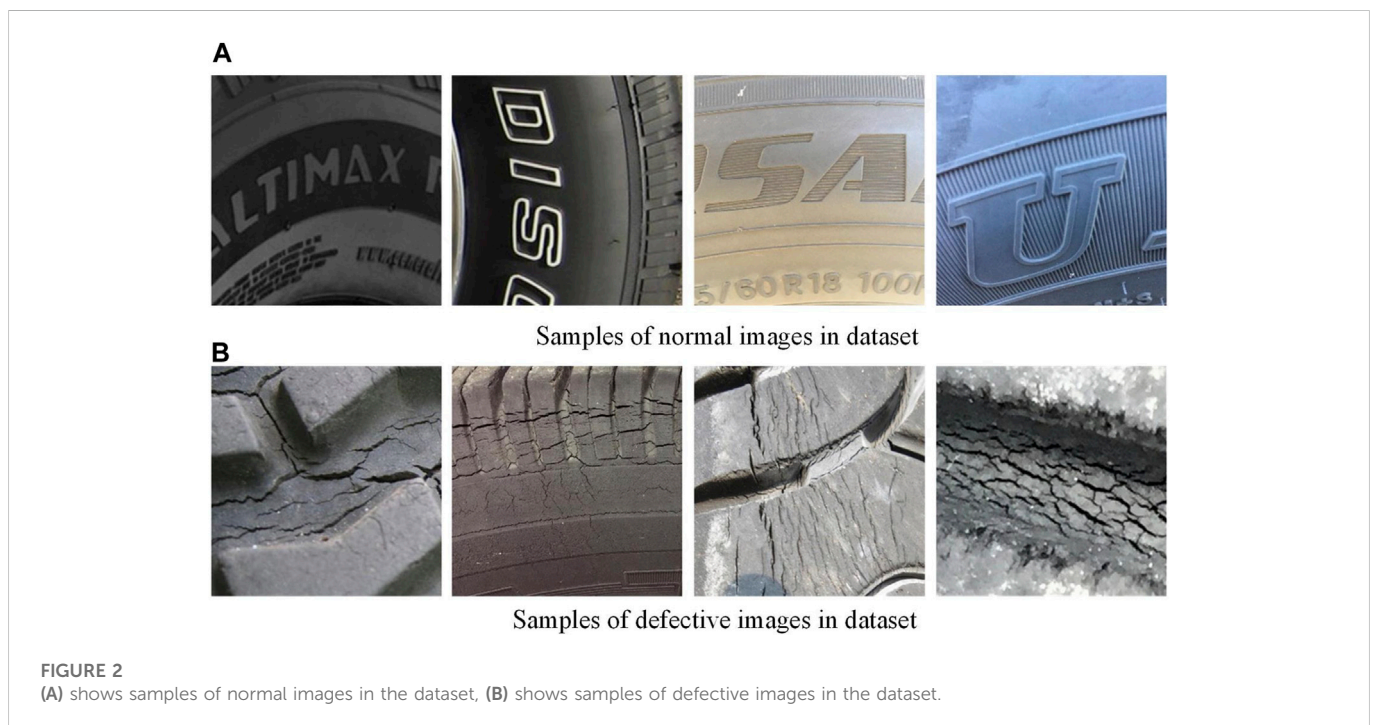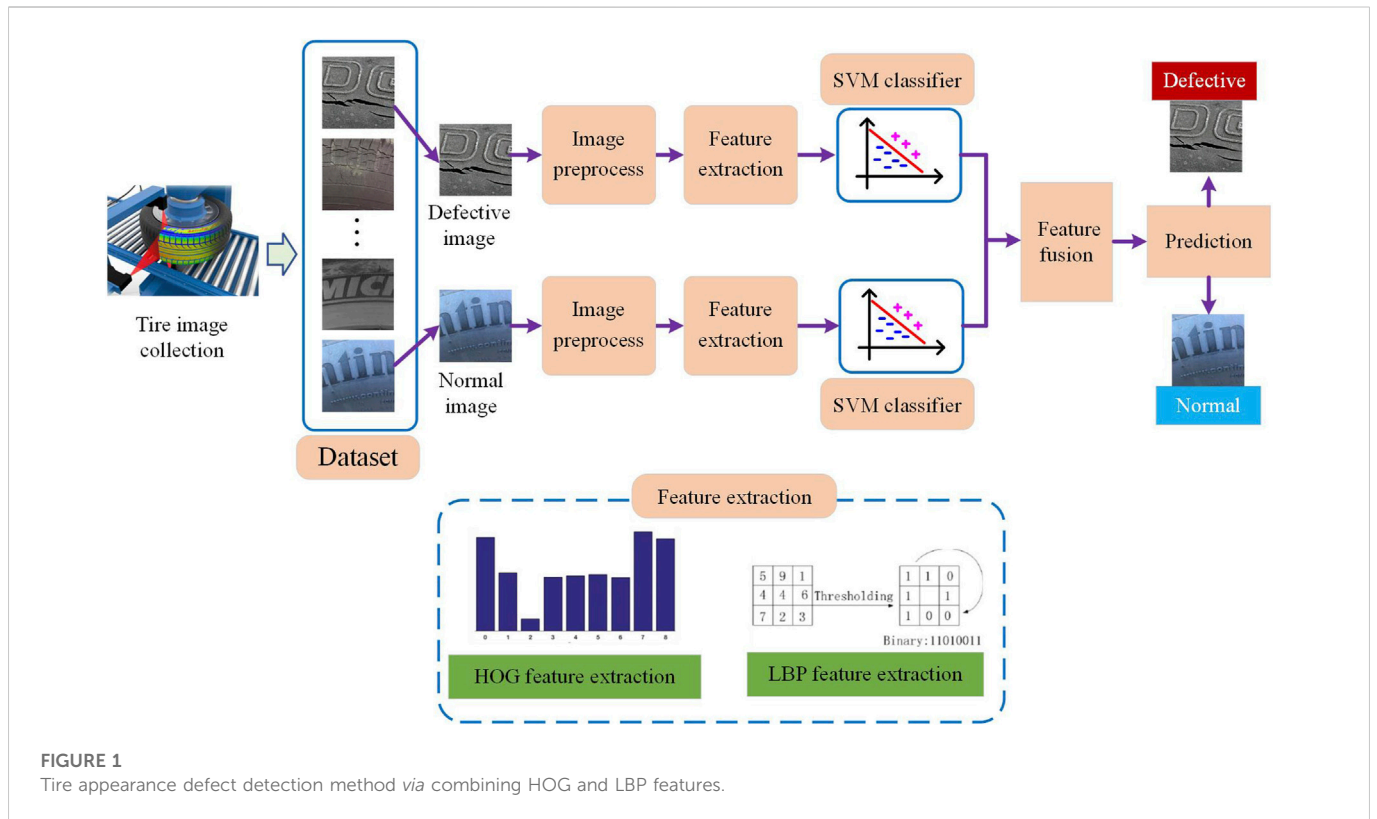
This dataset is mainly designed for a type of tire crack defect. Some tires in the picture collected from the network are not from the production workshop, and these tires are older. Since dust, dirt, or other sundries on tires interfere with defect detection, it is more difficult to accurately detect defects for these tires compared with tires in the production workshop. Some tire images in the dataset are shown in Figure 2. Using all pictures in the dataset, we can test the robustness and accuracy of the proposed tire defect detection method.

## 2.3 Image preprocess

To reduce the amount of computation and facilitate the extraction of tire image features, the paper preprocesses the tire image by using the weighted average gray-scale algorithm and the bilinear interpolation image size normalization algorithm.

### 2.3.1 The weighted average gray-scale algorithm

The color of every pixel in the image is composed of R (red), G (green), and B (blue) colors. Each component of these three color components is described with 255 values. If the feature is extracted directly from the original image, each pixel can produce more than

**FIGURE 1**
Tire appearance defect detection method *via* combining HOG and LBP features.



**FIGURE 2**
**(A)** shows samples of normal images in the dataset, **(B)** shows samples of defective images in the dataset.

16 million (i.e., 255³) parameters. These parameters easily lead to an exponential increase of computation in the process of feature extraction.

In this paper, the weighted average method is used for image gray processing, and different weights are used for the weighted average of RGB color components. The specific principles are interpreted as follows [22]:

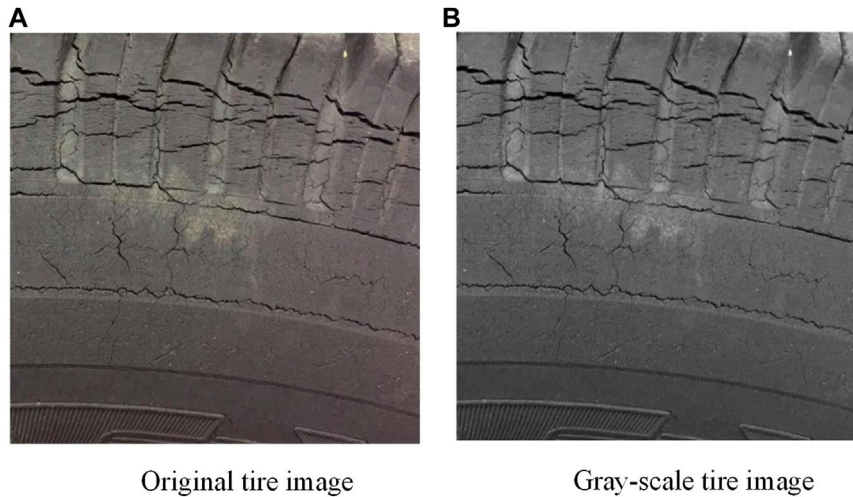$$I(x, y) = 0.299R(x, y) + 0.587G(x, y) + 0.144B(x, y), \quad (1)$$

**FIGURE 3**
**(A)** shows Original tire image, **(B)** shows Gray-scale tire image.
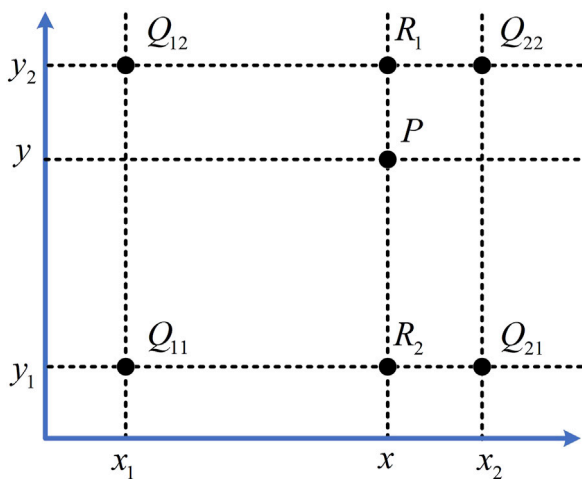


**FIGURE 4**
Schematic diagram of the bilinear interpolation method.

where $I(x, y)$ is the gray value of the pixel at the coordinate $(x, y)$; $R(x, y)$, $G(x, y)$, and $B(x, y)$ represent the value of R, G, and B components, respectively. Figure 3 shows the original tire image with defects and its gray-scale image. The gray-scale image and the original image are similar in texture structure and visual effect. However, the computational complexity of the gray-scale image is greatly reduced.

### 2.3.2 The image size normalization algorithm

If the image sizes for feature extraction are different, the dimensions of feature vectors will also be different. This difference disturbs the subsequent defect recognition because the similarity between feature vectors cannot be calculated. Therefore, it is necessary to normalize the sizes of the images in the dataset. In this paper, the bilinear interpolation algorithm is used to unify the sizes of all images in the dataset to $64 \times 64$ pixels.

The schematic diagram of bilinear interpolation is shown in Figure 4. The value of a new pixel interpolated point P is calculated by interpolating in the vertical $Y$ direction of $R_1$ and $R_2$, while the values of $R_1$ and $R_2$ are obtained by interpolating four pixels in the horizontal $X$ direction of $Q_{11}$, $Q_{12}$, $Q_{21}$, and $Q_{22}$, where the values of $Q_{11}$, $Q_{12}$, $Q_{21}$, and $Q_{22}$ are known in advance. In other words, the algorithm first employs the linear interpolation in the horizontal $X$ direction to obtain $I(R_1)$ and $I(R_2)$, and then, the pixel value $I(P)$ of point P is obtained by the linear interpolation from the vertical $Y$ direction. The implementation formula is described as follows [23]:

$$I(R_1) \approx \frac{x_2 - x}{x_2 - x_1} I(Q_{11}) + \frac{x - x_1}{x_2 - x_1} I(Q_{21}), \quad R_1 = (x, y_1), \quad (2)$$

$$I(R_2) \approx \frac{x_2 - x}{x_2 - x_1} I(Q_{12}) + \frac{x - x_1}{x_2 - x_1} I(Q_{22}), \quad R_2 = (x, y_2), \quad (3)$$

$$I(P) \approx \frac{y_2 - y}{y_2 - y_1} I(R_1) + \frac{y - y_1}{y_2 - y_1} I(R_2) \quad (4)$$

## 2.4 HOG feature extraction

The flowchart of the HOG feature extraction for the tire image is shown in Figure 5. The tire image is divided into several blocks without overlapping each other, and the block is then further divided into four cells. These cells and blocks are used to calculate HOG and LBP descriptors. In this section, we mainly interpret the HOG feature extraction process. LBP feature extraction is described in Section 2.5.

In the process of HOG feature extraction, the gamma transform of the target image is first used to reduce the influence of the illumination intensity change on image features, and then, the gradient operator is used to compute gradients of pixels. Afterward, our method calculates the cell's histogram with weighted projection statistics. Finally, all histograms are cascaded to construct the HOG feature of the whole tire image.

### 2.4.1 Computational gradients of pixels

The accurate extraction of the HOG feature is interfered by the change of the illumination intensity when the image is photographed.

**FIGURE 5**
HOG and LBP feature extraction flow.
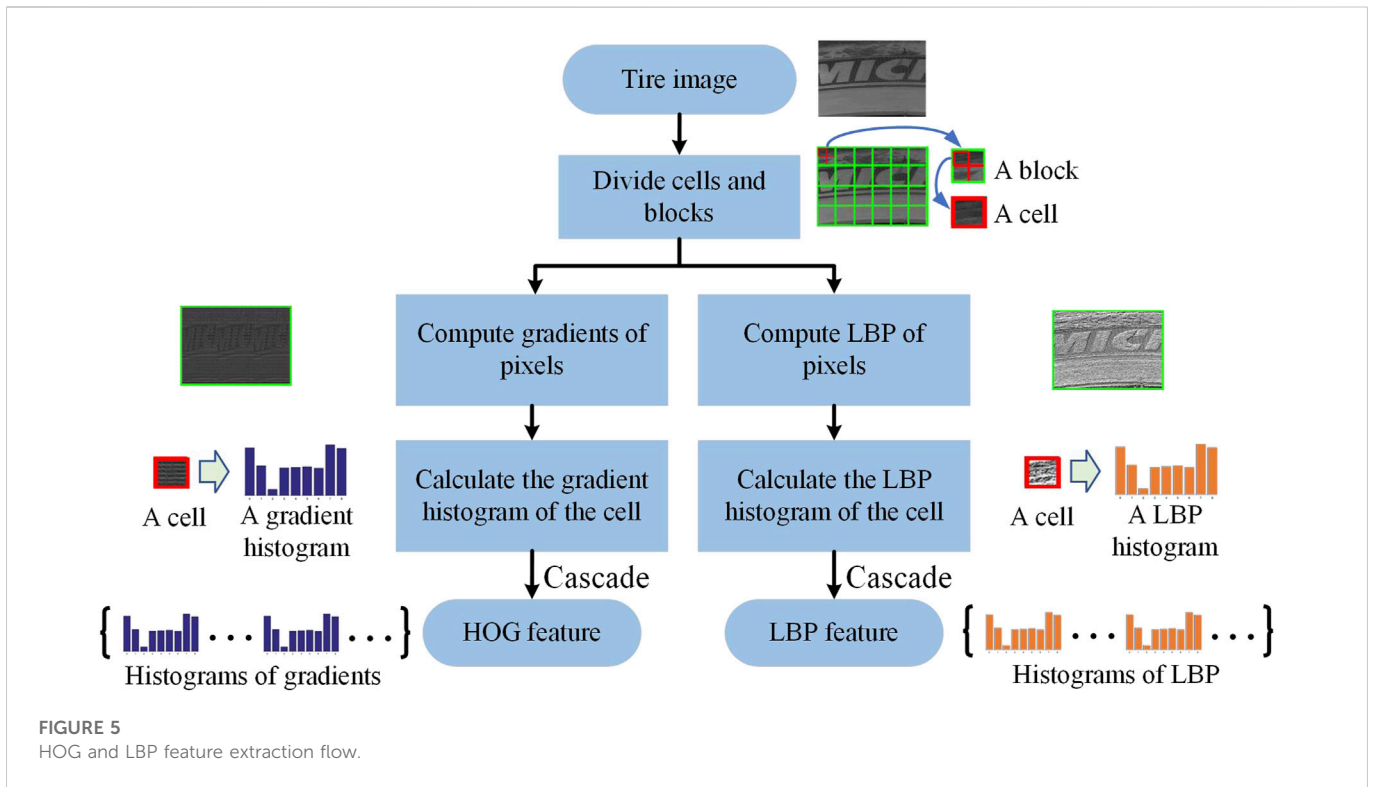
To overcome this problem, gamma is used to improve the illumination robustness of the tire image to reduce the influence of the illumination intensity change. Assuming the gamma value is 1/2, the gamma compression transformation formula is as follows [24]:

$$H(x, y) = H(x, y)^{gamma}, \qquad (5)$$

where $H(x, y)$ represents the pixel value at the coordinate $(x, y)$.

The gradient calculation formulas for the $X$ direction and $Y$ direction of the image are described in the following equations:

$$G_x(x, y) = H(x + 1, y) - H(x - 1, y), \qquad (6)$$

$$G_y(x, y) = H(x, y + 1) - H(x, y - 1), \qquad (7)$$

where $G_x(x, y)$ and $G_y(x, y)$ are the horizontal gradient and the vertical gradient of the pixel at the coordinate $(x, y)$, respectively.

The gradient amplitude and direction at the image pixel $(x, y)$ are calculated as follows:

$$G(x, y) = \sqrt{G_x(x, y)^2 + G_y(x, y)^2}, \qquad (8)$$

$$\alpha(x, y) = \tan^{-1}\left(\frac{G_y(x, y)}{G_x(x, y)}\right), \qquad (9)$$

where $G(x, y)$ and $\alpha(x, y)$ are the gradient amplitude and the direction at the image pixel point $(x, y)$, respectively. After calculating HOG gradients of all pixels in the image, we can obtain the HOG feature map.

### 2.4.2 Calculating the gradient histogram of the cell

Gradient directions and amplitudes of all pixels of the cell are counted to generate histograms. The horizontal axis of this histogram is the gradient direction, and the vertical axis is the gradient cumulative amplitude of each gradient direction interval. In general, the gradient direction ranges from 0° to 180°; it is divided into nine parts (bins) on average, i.e., any gradient direction bin = 20°.

Afterward, the cumulative sum of gradient amplitudes in each gradient direction bin is counted to obtain the eigenvector of each cell. This process is equivalent to mapping the pixels in the image to a corresponding angle range, and the weighted projection is carried out in the gradient direction histogram.

### 2.4.3 Obtaining the HOG feature

Each adjacent cell unit is combined into a large and spatially connected block, and then, the eigenvectors of each cell unit in the block are connected in a series to obtain the block descriptor. After eigenvectors of this block are normalized, we can obtain the HOG descriptor.

The final HOG feature of the tire image can be obtained by cascading all feature vectors in the block. Figure 6 shows the original image and gradient feature maps of normal and defective images.

## 2.5 LBP feature extraction

The local binary pattern (LBP) is an operator used to describe the local texture features of an image. The texture refers to the natural attribute of the surface of the object, which describes the distribution relationship between image pixels. The LBP feature does not change with the variation of the external illumination intensity.

### 2.5.1 Computation of the LBP of pixels

Figure 7 shows the flowchart of LBP feature extraction for the tire image. The basic idea of the LBP is to compare the gray value of an image pixel with the gray value of its surrounding pixels [25]. If the gray value of the surrounding pixels is greater than the gray
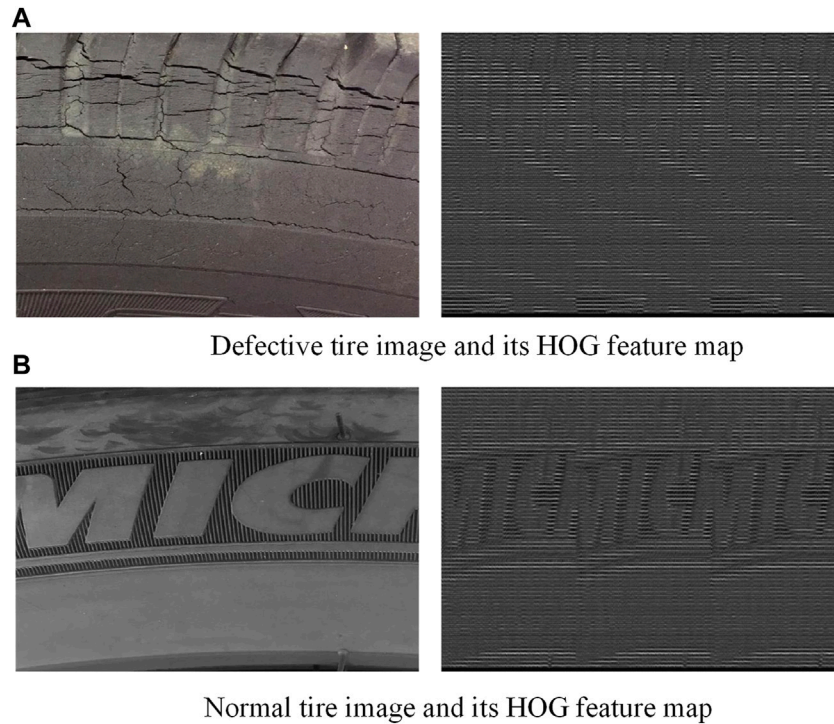
**FIGURE 6**
**(A)** shows defective tire image and its HOG feature map, **(B)** shows normal tire image and its HOG feature map.
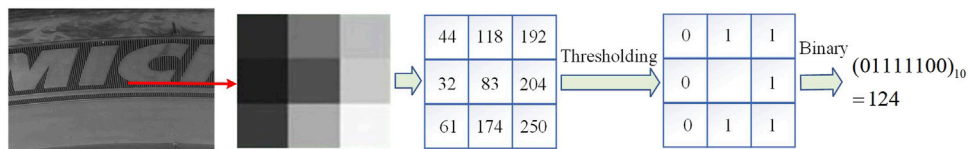


**FIGURE 7**
LBP descriptor calculation process.

value of the point, it is marked as 1; on the other hand, if the gray value of the surrounding pixel is less than the point, then it is marked as 0. The compared results are saved as a binary number, which is the LBP value of the point reflecting the local texture features of the image.

In our method, the basic LBP operator is used to calculate the LBP value of each pixel for the pre-processed tire image. The gray value of each pixel is compared with the gray value of the surrounding $3 \times 3$ neighborhood. If the gray value of the pixel larger than the center point is marked as 1, then the gray value of the pixel smaller than the center point is marked as 0. The result is saved as a binary number. After calculating LBP descriptors of all pixels in the image, we can obtain the LBP feature map.

### 2.5.2 Calculating the LBP histogram of the cell

The LBP image is divided into non-overlapping blocks and cells. The histograms of all blocks and cells are calculated. Since there are 256 (i.e., $2^8$) possible values for LBP values, the horizontal coordinate values of the histogram, therefore, range from 1 to 256.

### 2.5.3 Obtaining the LBP feature

The LBP feature vectors of the whole tire image can be obtained by cascading LBP features of each region block. Figure 8 shows LBP feature maps of the normal tire image and the defective tire image.

## 2.6 SVM classifier

After extracting HOG and LBP features, this paper, respectively, uses the two features to train SVM classifiers to get the prediction probability values for feature fusion.

The idea of the SVM classifier is that if the original data cannot be classified effectively in a low dimension, then the original data samples can be mapped to a higher or even infinite dimension feature space by the non-linear mapping algorithm. Then, the linear indivisible problem of the original space can be transformed into a linear separable problem in the high-dimension space.
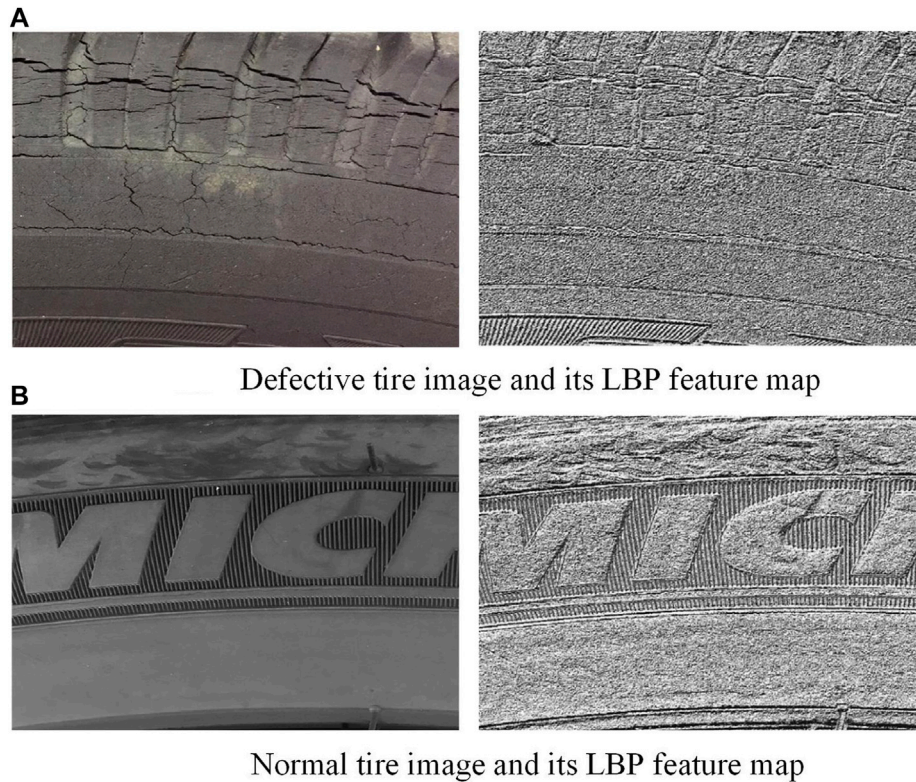
**FIGURE 8**
**(A)** shows defective tire image and its LBP feature map, **(B)** shows normal tire image and its LBP feature map.

To design SVM with a better classification performance, it is necessary to choose an appropriate kernel function. In this paper, the linear kernel function is selected for the case of linear separability [26]:

$$K(x_i, x_j) = \langle x_i, x_j \rangle. \tag{10}$$

The non-kernel functions selected for the linear indivisibility are as follows:

1) The polynomial kernel function:

$$K(x_i, x_j) = (\langle x_i, x_j \rangle + 1)^q. \tag{11}$$

This is a polynomial classifier of order $q$. $q$ generally takes 1–10 values.

2) The radial basis kernel function:

$$K(x_i, x_j) = \exp\left(\frac{|x_i - x_i|}{-\sigma^2}\right), \tag{12}$$

where sigma is generally selected from .001 to .006.

The cross-validation method is employed to select the kernel function. Cross-validation uses different kernel functions to train original samples until a kernel function with the smallest error is obtained.

Using the SVM classifier to test the tire image, our method outputs the prediction scores to classify the tire image as a normal image or defective image. The SVM prediction scores using HOG and LBP features are recorded as $Score_{HOG}$ and $Score_{LBP}$, respectively. Each score is a vector with the length of 2. The first and second score values in the vector, respectively, represent the possibility score that the image is classified into a defective or normal image. The larger the score value, the greater is the probability that the tire image belongs to the corresponding category.

## 2.7 Fusion of HOG and LBP features

The HOG and LBP feature can, respectively, describe the shape and texture information, but the tire appearance image consists of complex semantic information, and the observation contained by one feature alone has limitations. Therefore, HOG and LBP features are fused to build a relatively comprehensive tire feature model.

The additive fusion method is used to combine HOG and LBP feature prediction scores, and this prediction score fusion considers the shape and texture information comprehensively. The additive fusion is chosen according to the characteristics of the SVM classifier score. We do not utilize multiplicative fusion because the SVM classifier score may be zero. Multiplying zero with any score still equals zero, which may interfere with the correct judgment in multiplicative fusion. In other words, the non-zero similarity score may be changed to zero after multiplicative fusion; however, this zero score may be wrongly classified, which reduces the defect detection accuracy. In comparison, additive fusion can reduce the influence of the zero value, so we select the additive fusion method in this paper. The additive fusion formula is as follows:

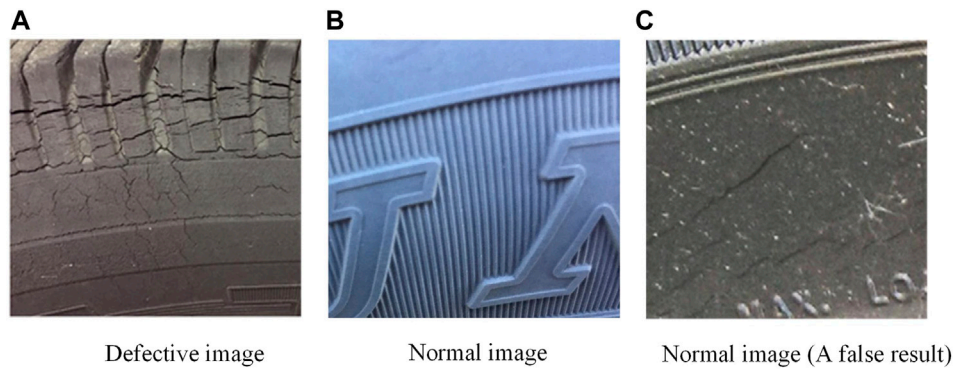$$Score = \lambda_1 \cdot Score_{HOG} + \lambda_2 \cdot Score_{LBP}, \tag{13}$$

**FIGURE 9**
**(A)** shows defective image detection result using the HOG + SVM algorithm, **(B)** shows normal image detection result using the HOG + SVM algorithm,
**(C)** shows a false result using the HOG + SVM algorithm.

where $Score$ is the prediction score after fusion, $\lambda_1$ and $\lambda_2$ represent the weight coefficients of HOG and LBP features, and $Score_{HOG}$ and $Score_{LBP}$ represent prediction scores of HOG and LBP features, respectively.

Finally, the input tire image is classified according to the score value, when the first element in $Score$ is larger than the second element; on the contrary, when the second element in $Score$ is greater than the first element, the input tire image is normal. The task of tire appearance defect detection is completed. We summarize the proposed method as Algorithm 1.

```
Input: Tire image dataset
   1:   Randomly select 80% of tire images in the dataset as
        training samples and the other 20% as testing
        samples;
   2:   Extract the HOG and LBP features of the training
        samples;
   3:   Train the SVM classifier using HOG and LBP
        features;
   4:   for i = 1 to I do
   5:      Extract the HOG and LBP features of the i th
           testing sample;
   6:      Calculate the SVM probability scores of HOG and
           LBP features for the testing sample;
   7:   Fuse the probability scores of HOG and LBP features
        according to Eq. 13;
   8:   Determine the classified result of the i th testing
        sample.
   9:   end for
Output: Defect detection result: Whether the testing
sample is normal or detective.
```

**Algorithm 1** Our proposed tire image defect detection method.

# 3 Experimental results and analysis

In this paper, we test our method on the formulated dataset, and the effectiveness and accuracy of the algorithm is verified.

In the experiments, we randomly assign 80% (i.e., 817 images) of 1,021 tire images as training sets and 20% (i.e., 204 images) as test sets.

The experiment is based on the MATLAB platform. The computer processor is Intel Core i7 2.3 GHz, and the memory is 16 GB.

To verify the improvement of fusing HOG and LBP features for tire defect detection methods, the defect detection results and accuracies of the following three algorithms are compared and analyzed:

1) HOG + SVM: Using the HOG feature and SVM classifier to realize tire image defect detection.
2) LBP + SVM: Using the LBP feature and SVM classifier to realize tire image defect detection.
3) HOG + LBP + SVM: Fusing HOG and LBP features and then combining the SVM classifier to realize tire image defect detection.

## 3.1 HOG + SVM tire defect detection method

We implement the HOG + SVM algorithm for tire images. Figure 9 shows the detection results and the corresponding original image. The results show that the HOG + SVM algorithm can detect the defective and normal image correctly, as shown in Figures 9A,B. However, some defective images are prone to be determined as normal images easily, which generates a false result, as shown in Figure 9C. It is because that the HOG only describes the edge information on the tire, defects such as cracks are easily regarded as tire patterns. To verify the ability of the HOG + SVM algorithm, the accuracy of the defect detection method is computed. The accuracy is formulated as follows:

$$Accuracy = \frac{N_{\text{correct}}}{N_{test}}, \tag{14}$$

where $N_{\text{correct}}$ is the correct defect detection sample number and $N_{\text{test}}$ is the total sample number in the test stage. We train and test 10 times for HOG + SVM algorithm. In each epoch, the detection results and accuracies are saved.

Table 1 shows the tire image defect detection accuracies of the HOG + SVM algorithm. The experimental results show that the recognition rate of the tire appearance defect detection by the HOG feature combined with the SVM classifier is about 70%. Although it can effectively detect some defects, it is far from enough for the desired effect in actual production. This method has a higher accuracy when detecting normal images, but there are still errors when detecting defective images, as shown in Figure 9.

**TABLE 1** Tire image defect detection accuracy of the HOG + SVM algorithm.

| Experimental label | 1 | 2 | 3 | 4 | 5 | 6 | 7 | 8 | 9 | 10 | Mean |
|---|---|---|---|---|---|---|---|---|---|---|---|
| Accuracy (%) | 70.5 | 68.6 | 72.6 | 71.5 | 72.5 | 67.2 | 71.5 | 72.9 | 68.2 | 69.3 | 70.5 |
| Running time (s) | .40 | .42 | .34 | .39 | .36 | .35 | .37 | .38 | .34 | .34 | .37 |



**FIGURE 10**
**(A)** shows defective image detection result using the LBP + SVM algorithm, **(B)** shows normal image detection result using the LBP + SVM algorithm.
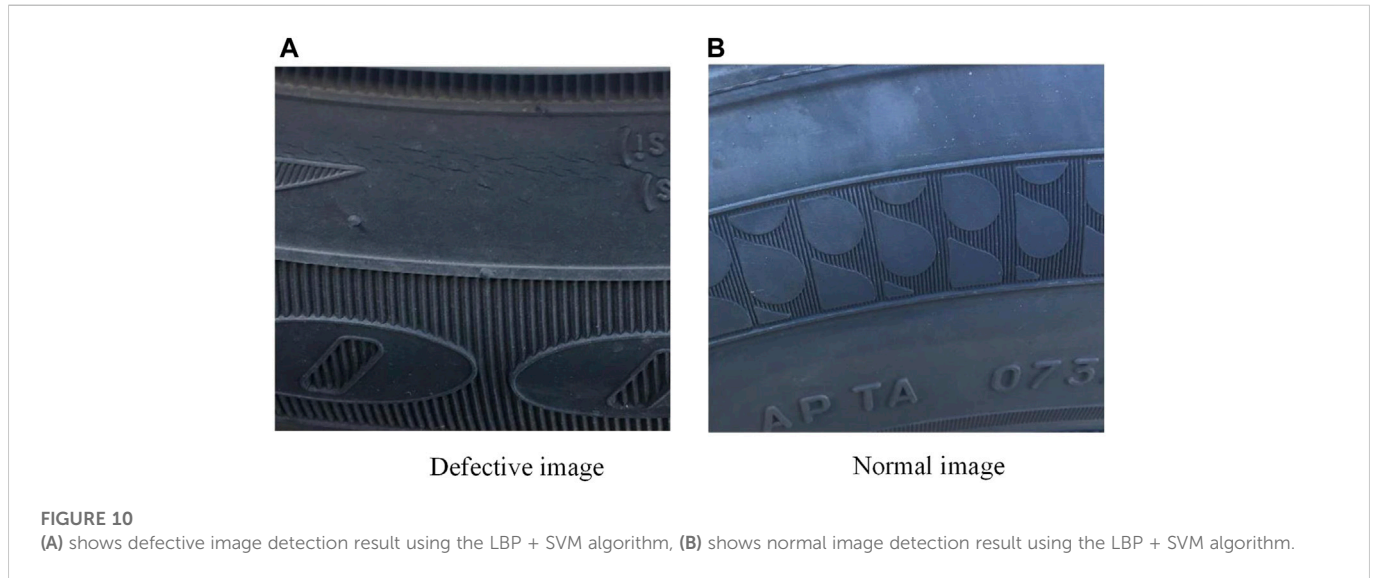
**TABLE 2** Tire image defect detection accuracy of the LBP + SVM algorithm.

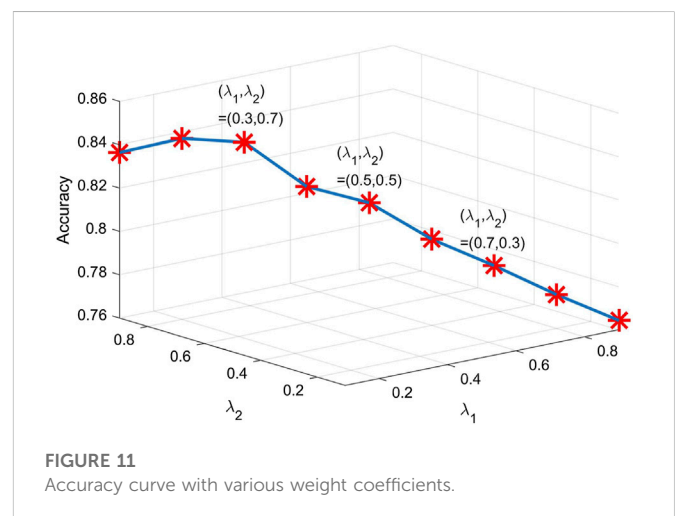| Experimental label | 1 | 2 | 3 | 4 | 5 | 6 | 7 | 8 | 9 | 10 | Mean |
|---|---|---|---|---|---|---|---|---|---|---|---|
| Accuracy (%) | 82.6 | 82.6 | 82.5 | 82.0 | 82.2 | 82.2 | 82.8 | 82.9 | 82.9 | 82.3 | 82.5 |
| Running time (s) | .40 | .41 | .45 | .35 | .41 | .35 | .35 | .36 | .34 | .36 | .38 |

## 3.2 LBP + SVM tire defect detection method

We implement the LBP + SVM algorithm for tire images. Figure 10 shows the detection results and the corresponding original image. The results show that the LBP + SVM algorithm can detect the defect image correctly, as shown in Figure 10.

Table 2 shows the tire image defect detection accuracies of the LBP + SVM algorithm. Compared with HOG + SVM, the LBP + SVM algorithm obtains higher detection accuracy. The accuracy of the LBP + SVM algorithm is higher than 12%. We think that the LBP is mainly used to describe texture features of the tire; the texture feature has a more discriminative ability for classifying the tire defect. Once a defect occurs, the LBP feature can clearly show the texture features of the image, and even small cracks can be detected.

## 3.3 HOG + LBP + SVM tire defect detection method

### 3.3.1 Fusion parameters

According to Eq. 13, the additive fusion method consists of two important parameters, i.e., $\lambda_1$ and $\lambda_2$, which represent the weight



**FIGURE 11**
Accuracy curve with various weight coefficients.

coefficients of HOG and LBP features, respectively. To select the optimal weight coefficient values, we draw the accuracy curve with different $\lambda_1$ and $\lambda_2$ values, as shown in Figure 11.
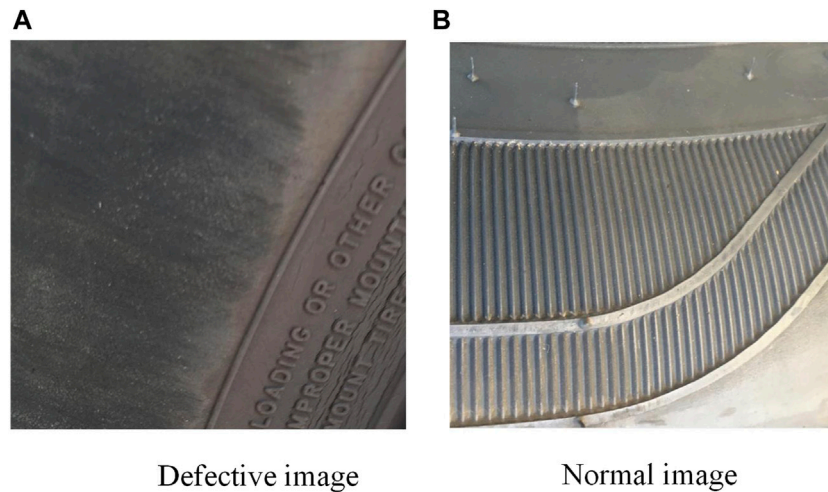
**FIGURE 12**
**(A)** shows defective image detection result using the HOG + LBP + SVM algorithm, **(B)** shows normal image detection result using the HOG + LBP + SVM algorithm.

**TABLE 3 Tire image defect detection accuracy of the HOG + LBP + SVM algorithm.**

| Experimental label | 1 | 2 | 3 | 4 | 5 | 6 | 7 | 8 | 9 | 10 | Mean |
|---|---|---|---|---|---|---|---|---|---|---|---|
| Accuracy (%) | 84.0 | 84.3 | 84.5 | 84.0 | 84.0 | 84.2 | 84.2 | 84.1 | 84.0 | 83.5 | 84.1 |
| Running time (s) | 1.13 | 1.06 | .79 | .73 | .95 | .70 | .69 | .70 | .70 | .72 | .82 |

If it is assumed that $\lambda_1 + \lambda_2 = 1$, then the value of $\lambda_2$ decreases with increasing $\lambda_1$. Figure 11 shows that the accuracy increases first and achieves the highest when $\lambda_1 = .2$; afterward, the accuracy begins to decrease when $\lambda_1$ is greater than .3. The reason is that the tire appearance has many types of textures, of which the LBP feature can better describe tire image than the HOG feature. Therefore, when $\lambda_1$ is less than .3, the accuracy is higher because the weight of the LBP feature is bigger than that of the HOG feature; on the contrary, when $\lambda_1$ is more than .3, the accuracy is lower because the weight of the LBP feature is smaller than that of the HOG feature. In one word, $\lambda_1 = .3$ can be considered as a critical threshold. We select this critical threshold as the optimal value of $\lambda_1$. Therefore, the values of $\lambda_1$ and $\lambda_2$ are set to .3 and .7 in our experiments, respectively.

### 3.3.2 Tire defect detection results

The detection images and defect results are shown in Figure 12 and Table 3. The experimental results show that our proposed HOG + LBP + SVM algorithm can correctly detect the defective and normal tire image. Moreover, the detection accuracy based on HOG + LBP + SVM is about 84%. The mean accuracy of the HOG + LBP + SVM is 1.6% and 13.6% higher than that of HOG + SVM and LBP + SVM algorithms, respectively. These results verify the effectiveness of combining the HOG feature and the LBP feature. The proposed method can complement the advantages of HOG and LBP features, and the edge and texture features of the tire image are comprehensively utilized to detect tire appearance defects.

In addition, we list the running time of the three algorithms in Tables 1–3 to analyze the speed of our proposed method. When compared to the algorithm only using the HOG or LBP feature, the combined algorithm needs more running time. In other words, feature fusion really increases the computational complexity. However, the significance of the improving accuracy is more important than the influence of the increasing time in some applications. Certainly, we will further optimize the algorithm structure to improve the calculation speed, and it is believed that the increased running time with the milliseconds level can be accepted under the rapid development of the GPU computing ability.

## 4 Conclusion

The paper proposes a tire defect detection method based on the fusion of HOG and LBP features. First, we establish a tire image dataset that consists of normal and defective tire images. Then, tire images are grayed and normalized to reduce the computational complexity and enhance the image quality. Afterward, the HOG feature and LBP feature are extracted and used to train the SVM classifier. Finally, the tire images are classified into the normal or defective image by fusing the prediction scores of HOG and LBP features. The experimental results show that our proposed method can effectively detect tire appearance defects. Compared to algorithms only using the HOG or LBP feature, the proposed method obtains higher detection accuracy.

## Data availability statement

## Author contributions

## Funding

## Conflict of interest

## Publisher's note

## References

1. Zhang Y, Wang Y, Jiang Z, Liao F, Zheng L, Tan D, et al. Diversifying tire-defect image generation based on generative adversarial network. *IEEE Trans Instrumentation Meas* (2022) 71:1–12. doi:10.1109/tim.2022.3160542

2. Zhang Y, Wang Y, Jiang Z, Zheng L, Chen J, Lu J. Tire defect detection by dual-domain adaptation-based transfer learning strategy. *IEEE Sensors J* (2022) 22(19):18804–14. doi:10.1109/jsen.2022.3201201

3. Zhu Q, Ai X. The defect detection algorithm for tire x-ray images based on deep learning. In: IEEE International Conference on Image, Vision and Computing; 27-29 June 2018; Chongqing, China (2018). p. 138–42. doi:10.1109/ICIVC.2018.8492908a

4. Wang R, Guo Q, Lu S, Zhang C. Tire defect detection using fully convolutional network. *IEEE Access* (2019) 7:43502–10. doi:10.1109/access.2019.2908483

5. Zhang Y, Li T, Li Q. Defect detection for tire laser shearography image using curvelet transform based edge detector. *Opt Laser Technol* (2013) 47:64–71. doi:10.1016/j.optlastec.2012.08.023

6. Zhang Y, Li T, Li QL. Detection of foreign bodies and bubble defects in tire radiography images based on total variation and edge detection. *Chin Phys Lett* (2013) 30(8):084205. doi:10.1088/0256-307x/30/8/084205

7. Sun H, Gu N, Lin C. Tire impurity defect detection based on grayscale correction and threading method. In: IEEE International Conference on Computer and Communication Systems; 23–26 April 2021; Chengdu, China (2021). p. 229–33.

8. Cheng J, Liu A, Tian T. Tire defect detection algorithm based on multi-task learning and normal feature fusion. In: International Conference on Computer Graphics, Artificial Intelligence, and Data Processing; 24–26 December 2021; Harbin, China (2021). p. 415–22.

9. Shabir MA, Hassan MU, Yu X, Li J. Tyre defect detection based on GLCM and Gabor filter. In: International Multitopic Conference; 29-30 November 2019; Islamabad, Pakistan (2019). p. 1–6. doi:10.1109/INMIC48123.2019.9022777

10. Saleh RAA, Konyar MZ, Kaplan K, Ertunç HM. Tire defect detection model using machine learning. In: 2022 2nd International Conference on Emerging Smart Technologies and Applications; 25-26 October 2022; Ibb, Yemen (2022). p. 1–5. doi:10.1109/eSmarTA56775.2022.9935140

11. Lin C, Chen G, Zhang Y, Sun F. Automatic detection of shoulder bending defects in tire X-ray images. In: International Conference on Computer Engineering and Applications; 18-20 March 2020; Guangzhou, China (2020). p. 877–81. doi:10.1109/ICCEA50009.2020.00193

12. Chen J, Li Y, Zhao J. X-ray of tire defects detection via modified faster R-CNN. In: International Conference on Safety Produce Informatization; 28-30 November 2019; Chongqing, China (2019). p. 257–60. doi:10.1109/IICSPI48186.2019.9095873

13. Pahinkar A, Mohan P, Mandal A, Krishnamoorthy A. Faster region based convolutional neural network and VGG 16 for multi-class tyre defect detection. In: International Conference on Computing Communication and Networking Technologies; 06-08 July 2021; Kharagpur, India (2021). p. 01–7. doi:10.1109/ICCCNT51525.2021.9579855

14. Li P, Dong Z, Shi J, Pang Z, Li J. Detection of small size defects in belt layer of radial tire based on improved faster R-CNN. In: International Conference on Information Science and Technology; 21-23 May 2021; Chengdu, China (2021). p. 531–8. doi:10.1109/ICIST52614.2021.9440580

15. Tao J, Zhu Y, Liu W, Jiang F. Smooth surface defect detection by deep learning based on wrapped phase map. *IEEE Sensors J* (2021) 21(14):16236–44. doi:10.1109/jsen.2021.3076610

16. Yang H, Wang Y, Hu J, He J, Yao Z, Bi Q. Segmentation of track surface defects based on machine vision and neural networks. *IEEE Sensors J* (2021) 22(2):1571–82. doi:10.1109/jsen.2021.3133280

17. Guo R, Liu H, Xie G, Zhang Y. Weld defect detection from imbalanced radiographic images based on contrast enhancement conditional generative adversarial network and transfer learning. *IEEE Sensors J* (2021) 21(9):10844–53. doi:10.1109/jsen.2021.3059860

18. Mohan P, Pahinkar A, Karajgi A, Kumar LD, Kasera R, Gupta AK, Nar SJ. Multi-contrast convolution neural network and fast feature embedding for multi-class tyre Defect Detection. In: International Conference on Electronics, Communication and Aerospace Technology; 05-07 November 2020; Coimbatore, India (2020). p. 1397–405. doi:10.1109/ICECA49313.2020.9297615

19. Sa'idah S, Fany A, Suparta IPYN. Convolutional neural network GoogleNet architecture for detecting the defect tire. In: International Conference on Computer Science and Software Engineering; 15-17 March 2022; Duhok, Iraq (2022). p. 331–6. doi:10.1109/CSASE51777.2022.9759694

20. Zheng Z, Yang H, Zhou L, Yu B, Zhang Y. HLU²-Net: A residual U-structure embedded U-Net with hybrid loss for tire defect inspection. *IEEE Trans Instrumentation Meas* (2021) 70:1–11. doi:10.1109/tim.2021.3126847

21. Zheng Z, Zhang S, Shen J, Shao Y, Zhang Y. A two-stage CNN for automated tire defect inspection in radiographic image. *Meas Sci Technol* (2021) 32(11):115403. doi:10.1088/1361-6501/ac13f8

22. Kumar K, Li JP, Shaikh RA, Ahmed R. Content based image retrieval using gray scale weighted average method. *Int J Adv Comput Sci Appl* (2016) 7(1). doi:10.14569/ijacsa.2016.070101

23. Kirkland EJ. Bilinear interpolation. In: *Advanced computing in electron microscopy*. Boston, MA: Springer (2010). p. 261–3.

24. Huang J, Haq IU, Dai C, Khan S, Nazir S, Imtiaz M. Isolated handwritten Pashto character recognition using a K-NN classification tool based on zoning and HOG feature extraction techniques. *Complexity* (2021) 2021:1–8. doi:10.1155/2021/5558373

25. Zeebaree DQ, Abdulazeez AM, Zebari DA, Haron H, Nuzly Abdull Hamed H. Multi-level fusion in ultrasound for cancer detection based on uniform LBP features. *Comput Mater Continua* (2021) 66(3):3363–82. doi:10.32604/cmc.2021.013314

26. Mohammadi M, Rashid TA, Karim SHT, Aldalwie AHM, Tho QT, Bidaki M, et al. A comprehensive survey and taxonomy of the SVM-based intrusion detection systems. *J Netw Comput Appl* (2021) 178:102983. doi:10.1016/j.jnca.2021.102983